Optics & Laser Technology 157 (2023) 108669

Contents lists available at ScienceDirect

Optics and Laser Technology

journal homepage: www.elsevier.com/locate/optlastec

Full length article

Gold-coated split laser-induced periodic surface structures as refractometric sensors

Alejandro San-Blas [a,b], Mahmoud H. Elshorbagy [c,d], Santiago M. Olaizola [a,b], Luis M. Sanchez-Brea [d], Ainara Rodríguez [a,b], Jesús del Hoyo [d], Eduardo Granados [e], Angela Soria-Garcia [d], Veronica Pastor-Villarrubia [d], Javier Alda [d,*]

[a] Ceit-Basque Research and Technology Alliance (BRTA), Manuel Lardizabal 15, Donostia/San Sebastián, 20018, Spain
[b] Universidad de Navarra, Tecnun, Manuel Lardizabal 13, Donostia/San Sebastián, 20018, Spain
[c] Physics Department, Faculty of Science, Minia University, El Minia, 61519, Egypt
[d] Applied Optics Complutense Group, Optics Departament, Faculty of Physics, Universidad Complutense de Madrid, Plaza de las Ciencias S.N, Madrid, 28040, Spain
[e] CERN, Esplanade des Particules 1217, Geneve, Switzerland

ARTICLE INFO

Keywords:
Plasmonics
Refractometric sensing
Fano resonances
Laser-induced periodic surface structures

ABSTRACT

The generation of surface plasmon resonances (SPR) in laser-induced periodic surface structures (LIPSS) allows their application in the field of optical sensing, such as the detection of refractive index variations in gases and liquids. We have fabricated gold-coated LIPSS nanostructures on stainless steel substrates by using femtosecond laser nano-ablation. This technique is a low-cost and high-throughput fabrication method applicable to fast and large-scale manufacturing. The depth profile of the fabricated LIPSS shows a central dip at the top of each ripple that split the geometry. The actual topography is modeled and included in a computational electromagnetism package to obtain the expected optical response under the experimental conditions. The measured and simulated spectral reflectances are compared, and the differences are explained by the departure of the fabricated LIPSS from the ideal topography. The experiments and simulations showed excellent agreement for the main spectral characteristics, like the Fano-like lineshapes of the spectral reflectance. This fitting provides the values used to determine the refractometric performance of the fabricated device, that shows a sensitivity of 518 nm/RIU and a figure of merit of 32 RIU^{-1} for an aqueous analyte. Our experimental results show that the fabricated devices are competitive in terms of cost and simplicity when compared to existing devices with similar performance.

1. Introduction

Surface plasmon resonances (SPR) appear when there is a coupling between an electromagnetic wave and the oscillating electrons at the interface between negative and positive electric permittivity materials, usually a metal and a dielectric. This coupling results in an electromagnetic wave propagating along the boundary between both materials, which is very sensitive to material and environmental variations at either side of the interface [1]. In fact, many sensing applications are based on the strong dependence that exists between the SPR excitation wavelength and the refraction index of the surrounding medium (analyte). Because of this property, the use of SPR has become essential in the field of sensing, with well-established applications in refractometry [1,2] and detection of substances, in particular biochemical materials [3,4].

Multiple implementations for the excitation of SPR have been developed along the years. Some of these practical realizations use prisms [5], and fibers [1,6,7]. However, these implementations result in expensive fabrication and bulky equipment [8]. An increasingly popular alternative are diffraction gratings, where SPR excitation is enabled via Bragg scattering [5]. Although these types of sensors exhibit lower sensitivity compared to other implementations, they show promising miniaturization and integration capabilities [8].

Diffraction gratings manufactured with lithographic methods [9,10] involve several fabrication steps and are costly and time-consuming. As an alternative, the generation of Laser-Induced Periodic Surfaces Structures (LIPSS) take place in a single step fabrication process. This direct laser processing technique can generate periodic nanostructures on the surface of most materials under certain conditions of irradiation [11].

* Corresponding author.
E-mail address: javier.alda@ucm.es (J. Alda).

https://doi.org/10.1016/j.optlastec.2022.108669
Received 8 June 2022; Received in revised form 24 July 2022; Accepted 5 September 2022
Available online 18 September 2022

In recent years, laser nanostructuring techniques have been developed to the point that their yield, control over structure, and regularity have greatly improved. Consequently, they are now a viable alternative for many industrial applications [12].

LIPSS usually exhibit periods of tens or hundreds of nanometers [13], which makes them ideal for nanostructuring steel surfaces for advanced rheologic capabilities [14,15], and photonic applications involving light–matter interaction in the optical range. The morphology of LIPSS can be controlled mainly through the laser wavelength and polarization, using beam conformation, and also through the fluence and number of overlapping pulses employed in the processing, N [11]. LIPSS can be grouped generally as Low-Spatial Frequency LIPSS (LSFL), with period close to the wavelength of the laser source, and High-Spatial Frequency LIPSS (HSFL), with period much smaller than the laser wavelength [16]. LSFL are observed in a wide range of irradiation parameters in metals [17]. Additionally, for large values of N, splitting of LSFL (usually termed split-LIPSS) can be observed. In this process, LSFL are initially formed, and the subsequent pulses interact with the nanostructures, dividing each ripple in two.

In this work, we present the fabrication of a sensing device based on split-LIPSS and demonstrate its application in refractometry. Firstly, we provide the details about the fabrication of the device, its morphological characterization with diverse microscopy techniques, the method followed in its optical characterization, and the description of the computational simulations carried for comparison with the experimental results. Then, the plasmonic behavior of the device using water as analyte is examined for different incident angles. Finally, the refractive index sensing capabilities of the sensor are measured by modifying the refractive index of the analyte (salty water with different concentrations of NaCl).

2. Fabrication and characterization of refractometric LIPSS

A Ti:Sapphire laser emitting 120 fs pulses with a central wavelength $\lambda = 800$ nm at a repetition rate of 1 kHz was used for the generation of the nanostructures [18]. In this contribution, the laser beam was focused onto the surface of the sample through a cylindrical lens of focal length $f = 100$ mm (see Fig. 1). A variable attenuator consisting of a half-wave plate and a polarizing beam splitter was used to adjust the pulse energy (E). Another motorized half-wave plate was used to adjust the polarization of the laser beam so that it would be parallel to the translation axis. The movement of the sample was controlled with a motorized stage moving along the X-axis. The position of the sample along the beam propagation axis was controlled with another motorized stage with motion in the Z-axis. The size of the laser focal spot was measured with a CCD, showing a Gaussian distribution of energy with high ellipticity due to the cylindrical focusing. The gaussian widths of the beam were found to be $\omega_x = 54.5$ μm and $\omega_y = 6$ mm. As a result of this optical configuration, it is possible to process large areas in a single pass, achieving high regularity of LIPSS at high speed since no overlapping parallel passes are needed.

The irradiated material was stainless steel (AISI 304) with an average roughness of $R_a = 276.3$ Å. The stainless steel shows better LIPSS regularity than most other metals due to its short-ranged surface plasmon polaritons (SPPs) [19]. Before and after the laser processing, an acetone ultrasonic bath was applied to the sample for 3 min to remove dirt particles and debris adhered to the surface.

Femtosecond laser ablation generates LIPSS on stainless steel in a limited range of fluences. If the fluence is below 50 mJ/cm^2, there is not formation of LIPSS. For higher than 150 mJ/cm^2, the material is strongly ablated and LIPSS are erased. Within this range, an appropriate selection of the number of pulses splits the LIPSS. The fabricated sample was processed under irradiation conditions of $E = 0.55$ mJ pulse energy and $v = 0.625$ mm/s displacement speed. The surface of the stainless steel was positioned along the Z-axis so that the processing took place at the beam waist of the laser beam, in order to achieve higher regularity in the resulting nanostructures [18]. The sample was translated 30 mm under irradiation from the laser beam. Average fluence per pulse was calculated as $F = E/(\pi\omega_x\omega_y)$, and the overlapping number of pulses as $N = 2\omega_x/(vT)$, where $T = 1$ ms is the inter-pulse period of the laser. Therefore, in the presented sample, $F = 53.5$ mJ/ cm^2 and $N = 174$ pulses.

After laser irradiation, an Au coating was deposited on the surface of the sample through direct current (DC) sputtering. Au was chosen for its high reflectance and well-known plasmonic properties in the visible range [20,21]. The process took place at room temperature, with a constant vacuum pressure of 5μbar. The DC source used to ionize the Ar gas was set with a voltage of 400 V and a current of 0.25 A. In this process, we uniformly deposited onto the sample an Au layer increasing in thickness with time at an estimated rate of 0.49 nm/s. Therefore, the thickness of the gold layer can be set to any range by adjusting the duration of the deposition process. Since good adhesion between the stainless steel and the deposited Au had been observed, no adhesion layer was necessary. The thickness of the coating was chosen thick enough to fully cover all areas with Au. In consequence, a sputtering process with a duration of 630 s was performed, with an objective thickness of 300 nm.

The morphology of the resulting nanostructures was evaluated through scanning electron microscopy (SEM), both superficially and using the focused ion beam (FIB) technique, and Atomic force microscopy (AFM).

A comparison between the geometry of the nanostructures with and without Au coating is shown in Fig. 2. Before application of the Au coating (see the SEM image in Fig. 2.a), the generated nanostructures show high regularity, forming parallel lines across the length of the track (30 mm) that continue without interruption or bifurcation, with the exception of occasional imperfections, such as scratches on the surface. The 2D-FFT analysis (see Fig. 2.c) of this uncoated surfaces confirms the presence of highly regular LIPSS with a period of $\Lambda = 685 \pm 10$ nm. The periodicity is revealed by the symmetric sidebands around the central maximum (zero-frequency component). The distance between the central peak and the first peak defines the fundamental period of the grating. The relation between the intensities of the peaks give information about the morphology of the profile in the original micrograph. In this case, an intense fundamental frequency followed by a less intense second harmonic and negligible higher orders indicate the formation of type-2s LIPSS, also called split-LSFL [16]. Actually, split-LSFL have been reported to appear at similar values of F and N to those presented here [22] and their formation mechanism has been previously explained [16]. The presence of split-LIPSS is further confirmed in the micrographs obtained with the FIB technique (see Fig. 2.e). The darkest gray layer at the bottom of the image corresponds to the stainless steel layer. From this FIB image, the generated nanostructures present wide ripples with narrow valleys, with an average height of 115 ± 33 nm. The ripples also show a split profile with a dip at the center of the ripple, having a variable depth of a few tens of nanometers. The inhomogeneity in the profile between ripples is typical in the processing of LIPSS in metals due to the nature of their formation. Then, an averaged optical response is expected for large area illumination conditions. The period of LIPSS can be tuned with the parameters of irradiation. Namely, the laser wavelength marks the upper limit for the period of LSFL, in this case, 800 nm. As the number of pulses increases, the period decreases significantly [11]. The height of LIPSS depends on the specific LIPSS type, and for LSFL it is in the few hundreds of nanometers range [12]. With the introduction of the Au coating, no significant differences can be observed in the SEM micrograph or 2D-FFTs (see Fig. 2.b and d, respectively), other than a variation in the visual brightness of the surface.

The FIB profile shows a conformal Au coating, since the surface of the coating replicates the stainless steel profile underneath. The average thickness of the coating is 309 ± 16 nm. A close inspection of the coated

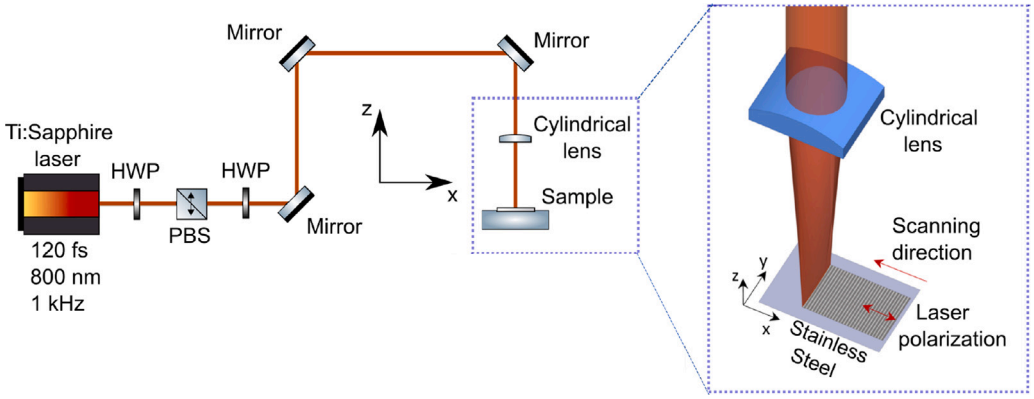

Fig. 1. Processing setup used for the generation of the gratings. Stainless steel samples were translated along the X-axis, with the resulting LSFL oriented perpendicular to the laser polarization. HWP: Half-wave plate, PBS: Polarizing beam splitter.

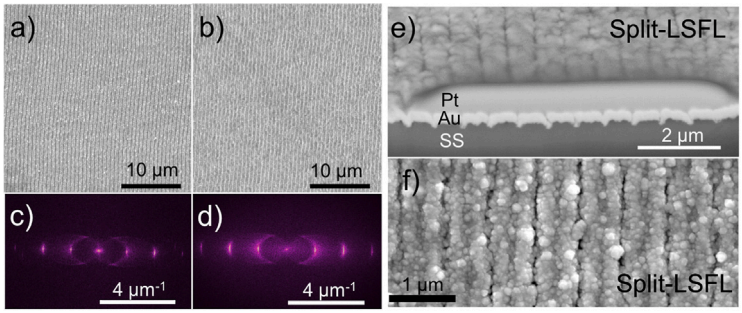

Fig. 2. Morphology of the fabricated nanostructures. SEM of the sample before (a) and after (b) Au deposition, with their respective 2D-FFT (c) and (d). (e) FIB section of the coated sample. Dark gray at the bottom of the image is the stainless steel (SS) substrate. On top of it, a light gray layer corresponding to the Au is observed. A platinum (Pt) coating was applied on the resulting surface as a step necessary in the FIB technique in order to protect the edge of the profile from the ion beam. (f) Large magnification SEM of the sample after Au deposit. The label split-LSFL has been added to the plots to denote the type of LIPSS formed.

sample (see Fig. 2.f) reveals the agglomeration of Au clusters with size in the order of tens of nanometers. Additionally, in this micrograph the splitting of LIPSS is more noticeable as the darker regions in the middle of each ripple are a clear indication of a deepening in profile height, although not as deep as the valleys between ripples.

AFM measurements (see Fig. 3.a) revealed features of the profile similar to the ones observed in the SEM and FIB micrographs. Several parallel scans, corresponding to the area between the red lines in Fig. 3.a were averaged in order to obtain a more regular profile (see Fig. 3.b).

The optical performance of the fabricated sample was examined by means of spectrophotometry. The reflectance of the gold-coated nanostructures was measured as a function of wavelength. The light source was a broadband (450–2400 nm) laser, NKT SuperK COMPACT, whose output was polarized at a variable polarization angle. The specular reflection was collected by an integrating sphere and then transmitted to the spectrometer. The polarization of the laser was chosen to be linear and perpendicular to the nanostructures, this is, with incident TM-polarization (see Fig. 4).

A cell was employed to host a variety of liquids (analytes) under test. In this configuration, we apply the Snell's law to correct the angle of incidence at the sample. This evaluation accounts for the change in direction of the beam at the air–cell and cell–liquid interfaces.

Our numerical calculations start from the morphological structure of the fabricated sample. The experimentally measured profile is used to build the geometry of the modeled design. A parametric profile based on trigonometric functions reproduces the split grating geometry obtained in the fabrication [23]:

$$h(x) = \begin{cases} 0, & \text{if } x \in A_1 \\ \frac{H_1}{2}\left[1 - 2\left(\frac{1+\cos(2\pi x/W_1)}{2}\right)^{\beta}\right] & \text{if } x \in A_2 \\ H_1 - H_2, & \text{if } x \in A_3 \end{cases}, \quad (1)$$

where $A_1 = [-\Lambda/2, -W_1/2) \cup [W_1/2, \Lambda/2)$, $A_1 = [-W_1/2, -W_2/2) \cup [W_2/2, W_1/2)$, and $A_1 = [-W_2/2, W_2/2)$ (the geometrical meaning of W_1, W_2, Λ, H_1 and H_3 are shown in Fig. 3.c). The profile of the surface in contact with the analyte is $h(x) + H_3$ (see Fig. 3.c). The control parameters of this shape are the power of the trigonometric function (flatness factor, $\beta = 2$), its period, $W_1 = 500$ nm, the period of the unit cell, $\Lambda = 685$ nm, and the height of the grating, $H_1 = 100$ nm. The split of the LIPSS is modeled as a rectangular dip having a width $W_2 = 137$ nm, and a depth $H_2 = 30$ nm, Finally, the LIPSS profile is coated with a conformal layer of gold having a thickness $H_3 = 300$ nm. These values have been obtained after fitting the actual measured profile with the profile model.

The optical model is generated using the finite element method (FEM) included in the simulation package COMSOL Multiphysics. The structure is illuminated by a tunable monochromatic light source where the angle of incidence is varied maintaining the TM excitation condition. The reflected light is collected by a corresponding port listening the mirror reflection. The structure is made of three main materials: analyte medium at the source and detector domains, a gold thin layer, and a stainless steel layer thick enough to avoid transmission through the structure. As the sample geometry is periodic, we reduce it to only one unit cell, and then apply Floquet boundary conditions on both sides of the unit cell to expand the solution over the real size of the sample. The whole model is terminated from top and bottom by perfect-matched layers (PMLs) to absorb higher order modes and prevent them from falsely interact with the incoming light and the low order diffraction modes of interest. The PML effective orientation is adjusted using both incident wavelength and angle to efficiently absorb radiation at the direction of interest.

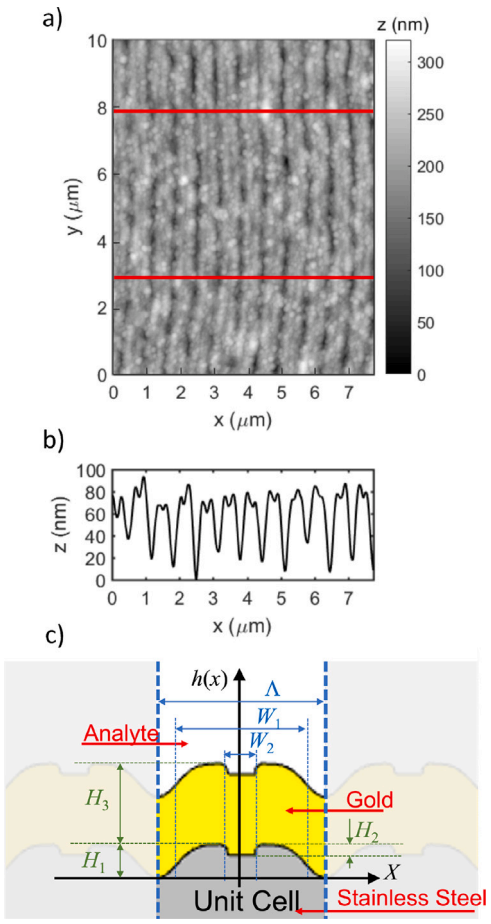

Fig. 3. (a) AFM scanning of a region of the fabricated sample. (b) Average profile of the LIPSS between the red lines in (a). (c) Profile used in the simulations.

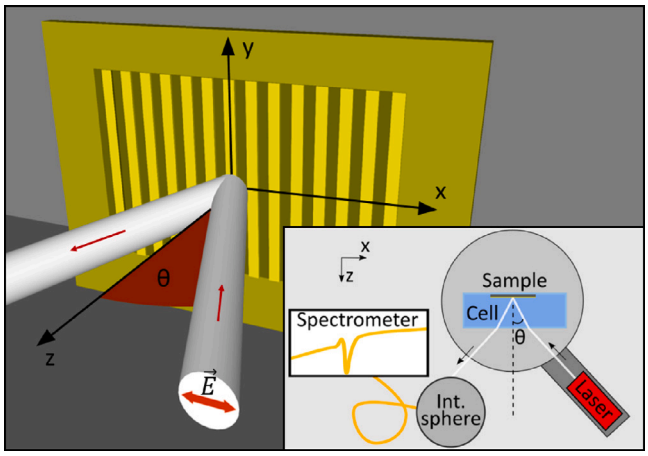

Fig. 4. Laser beam irradiating the fabricated sample. Inset: general scheme of the setup used in the optical characterization. The laser source is located on the arm of the θ–2θ, while the sample is at the center of the mechanism inside the cell.

3. Refractometry using LIPSS

First of all, we analyze the plasmonic response of the sample immersed in deionized water, at room temperature, and for various angles of incidence θ between 7° and 47° with incident TM-polarization. The minimum angle was limited by the optomechanical elements in the measurement setup blocking the reflected light, while the maximum angle was limited by the total internal reflection in the water–air interface, taking place at $\sim 48°$. The objective of these measurements was to find the incident angle that could report the best results for refractometric sensing.

The spectral reflectance of the samples was calculated as $R = R_s/R_0$. Here, R_0 is the reference reflectance, obtained by illuminating a silver mirror inside the water-filled cell. The experimental reflectance, R that varies between $R \sim 15\%$ and $R \sim 55\%$ in the measured range of λ (see Fig. 5.a). The spectral response of the structure shows an asymmetric line-shape derived from the excitation of Fano resonances. One of the simplest equation representing this interference can be written as the sum of the background r_{bk} plus a Lorentzian line-shape related to the SPR:

$$r_d = r_{\mathrm{bk}} + f\frac{\gamma}{(\omega-\omega_0)i+\gamma}, \tag{2}$$

where r_d is the complex amplitude of the Fano resonance, ω_0 is the resonant frequency of the SPR, γ is related with intrinsic losses due to material absorption and determines the spectral width of the SPR, and f is a complex-valued coefficient that describe the interference between the continuous background caused by diffraction and the SPR spectral variation [24]. In this contribution, the background term, r_{bk}, is expanded as a Taylor series around ω_0 up to the 3$^{\mathrm{rd}}$ order. When the reflectance shows several resonances, the SPR term is the addition of a number of Lorentzian profiles equal to the number of resonances appearing within the spectral range of interest.

On the other hand, the resonant wavelength λ_0 of the mode m for SPR generated by a periodic structure of period Λ when illuminated under oblique incidence at an angle θ, follows a dependence given by the matching condition [5]:

$$\sin(\theta) = -\left(\frac{m\lambda_0}{n_a\Lambda}\right) \pm \sqrt{\frac{\varepsilon'_m}{\varepsilon_a+\varepsilon'_m}}, \tag{3}$$

where n_a is the refractive index of the analyte (water in this case), ε_a is the permittivity of the analyte (a dielectric), and ε'_m is the real part of the permittivity of the metal (Au in the presented sample).

The experimental spectral reflectance shown in Fig. 5.a reveals two resonances at low angles, corresponding to the modes $m = +1$ and $m = -2$ in Eq. (3) and marked with squares (□) and diamonds (◇), respectively. The resonance in mode $m = +1$ blue-shifts, while in mode $m = -2$ it red-shifts. At $\theta \sim 23°$, the resonances from both modes merge in a single dip, which broadens the resulting profile. Simulations using the described structures and having water as the surrounding medium were also carried out for several incident angles (see Fig. 5.b). The results show a similar profile and behavior compared to the experimental ones. The calculated R shows deeper peaks than the experimental reflectance, reaching values between $R \sim 0\%$ and $R \sim 90\%$, which means sharper Fano resonances. This is due to the ideal periodic LIPSS actually simulated, meanwhile the experimental LIPSS have some degree of irregularity and the illuminated beam averages the geometry. Despite that, in the simulations we find the same modes and the same shifting behavior with θ as in the experimental reflectance.

Fig. 5.c represents the values of λ_0 and $\Delta\lambda$ obtained from the fitting of the experimental and simulated spectral reflectances to the Fano line-shape (see Eq. (2)) when $m = -2$. The central wavelength of the resonance, λ_0, for the experiment and the simulation match with a relative error of 1.5%, except for the angles between 15° and 27°. This angular range is where the red and blue shifting of the modes ($m = +1$ and $m = -2$, respectively) merge. Also the value of $\Delta\lambda$ changes its behavior in the same spectral range. The interaction between the profiles of the modes results in a change of the spectral reflectance, depending on the shape and relative position between the two resonances. After analyzing the experimental and simulated reflectances we conclude that, for angles larger than $\theta = 27°$, the resonant wavelength λ_0 increases linearly with θ, meanwhile $\Delta\lambda$ decreases. Then, we select $\theta = 46°$ as the angle of incidence for refractometric sensing.

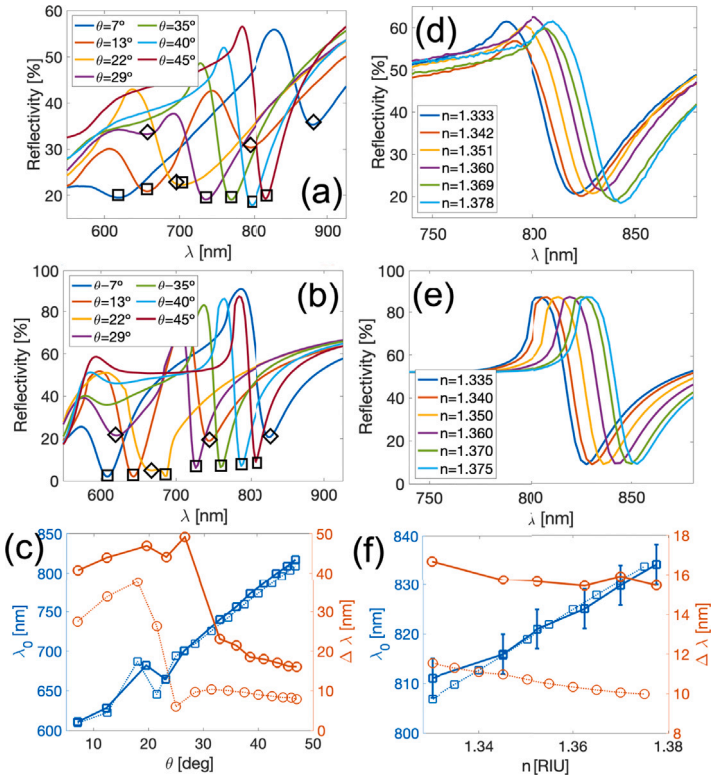

Fig. 5. Spectral reflectance of the sample for TM polarization, in terms of the angle of incidence (experimental (a), and simulated (b)), and the index of refraction of the analyte (experimental (d), and simulated (e)). In figures (a) and (b) the minima corresponding to modes $m = -2$ and $m = 1$ are marked with squares (□) and diamonds (⋄), respectively. Note that minimum reflectance does not take place at $\lambda = \lambda_0$, according to the Fano model. Plots (c) and (f) show the values of the central wavelength λ_0, (represented in blue with squares), and width $\Delta\lambda$ (represented in red with circles) obtained from the experiment (solid lines) and simulations (dotted lines) for mode $m = -2$. The plot in (c) correspond to the spectral reflectances shown in (a) and (b), and the plot in (f) are for the reflectances in (d) and (e). The experimental values for λ_0 in (e) are also affected by the marked error bars.

The influence of the refractive index of the surrounding medium on the resonant wavelength is measured through the sensitivity S, calculated as [25] $S = \partial\lambda_0/\partial n_a$. Additionally, the figure of merit (FOM), defined as [25] FOM $= S/\Delta\lambda$, is used to measure how sensitive the device is to a small variation in the composition of the analyte [26].

In order to test the sensing capabilities of the device in environments where the change in refractive index is small, the spectral reflectance of the device was measured using different concentrations of salty water (see Fig. 5.d-f). The concentration of salt by weight, C, was varied between 0% and 25% (just below the saturation level), in steps of 5%. The refractive index of this solution, n_s, increases linearly with C (expressed in percentage) as $n_s = 1.333 + 1.8 \times 10^{-3} C$ [27].

The spectral reflectance for all concentrations show a profile similar to the case $\theta = 45°$ in Fig. 5.a, since the incident angle and surrounding media are almost identical. In particular, in the spectral range shown in Fig. 5.d and e, $[740, 880]$ nm, a Fano resonance with the previously explained characteristics is observed, with maximum $R \sim 62\%$ and minimum $R \sim 18\%$. Different concentrations shift λ_0 (see solid blue lines in Fig. 5.f) from $\lambda_0 = 811$ nm to $\lambda_0 = 834$ nm as C (and its corresponding n_a) increases from 0% to 25%. The error bars associated to the experimental data of λ_0, with a value of ± 2.6 nm are obtained assuming an error in the incident angle of $\pm 0.5°$. This value was extracted from the study of the resonant wavelength in water with the incident angle (Fig. 5.c), which shows a variation of ~ 5 nm per degree in the $[40° - 45°]$ range of θ.

The simulations (see Fig. 5.e) show a very similar trend. As it happened with the spectral reflectance in terms of the angle of incidence, the variation in R is larger than in the experimental values, with maxima of $R \sim 90\%$ and minima of $R \sim 10\%$, which makes the resonance narrower. Here, the shift in λ_0 is linear, from $\lambda_0 = 807$ nm at $n = 1.330$ to $\lambda_0 = 834$ nm at $n = 1.375$. As it happened with the case presented in Fig. 5.c, the experimental resonances (see Fig. 5.f) are wider in the experiments than in the simulations, where $\Delta\lambda$ remains almost constant with an average value of 15.8 nm. The bandwidth obtained from simulations decreases very slightly with n_s, having an average of 10.7 nm. Both the sharper lineshape at λ_0 and smaller $\Delta\lambda$ are a consequence of the ideal periodicity of the geometry used in the simulations. With these values, the sensitivity of the fabricated sample working as a refractometric sensor was calculated to be $S^{\text{exp}} = 518$ nm/RIU, a value slightly lower compared to the simulations, $S^{\text{sim}} = 603$ nm/RIU. Additionally, FOM takes a value of 32 RIU^{-1} in our experiment, and 56 RIU^{-1} for the simulations. The difference in sensitivity between experimental and simulations is derived from experimental errors of our measurement set-up (see Fig. 5.f). The goniometric variables are affected by a small uncertainty, around $0.5°$, in the angular positioning of the sample that can influence the value of the angle of incidence θ. Additionally, the preparation of the salt and water solutions have some small, although not negligible, experimental error associated to it. For the sensitivity, the morphology of the nanostructures in the simulations should not play a role here, since sensitivity is related to the period Λ (from Eq. (3)) rather than to the specific shape, and the experimental error in Λ is estimated to be much lower than in θ or C. On the other hand, the higher values of FOM in the simulations are derived mainly from the difference in $\Delta\lambda$ (see Fig. 5.f). The wider resonances observed experimentally can be explained by the imperfections and irregularities of the fabricated nanostructures. As seen in Fig. 2.(d), period Λ is not found as a single value but instead as a distribution of periods centered around 685 nm with a FWHM of 10 nm. Therefore, while the optical behavior in the simulations is calculated for a fixed period, in the experiment, the response can be seen as a superposition of weighted responses that follows the statistical distribution of periods.

Besides the low cost and the high throughput fabrication advantages associated with LIPSS, the device presented in this contribution has a

comparable performance to similar recent approaches. For example, a gold-coated silicon grating fabricated by femtosecond laser shows a sensitivity of 10^{-7} g/cm^2 for uranium detection in aqueous media [28]. Another low cost refractometric sensors that uses the grooves of DVD discs as grating template give a spectral interrogation sensitivity of 514 nm/RIU when detecting NaCl, [29], and a value of 312 nm/RIU when sensing glucose concentration for a gold-coated DVD-R disc [30]. If silver is used, the resulting plasmonic structures make possible to detect changes in the index of refraction with FOM values of 13.5 RIU^{-1} and 5.24 RIU^{-1} for low and high glucose concentrations, respectively [31]. Large-scale gold-coated dielectric gratings have demonstrated a maximum measured sensitivity of 628 nm/RIU [32], and the excitation of high-Q SPR using an array of gold nanogrooves, shows a large value of FOM of 617 RIU^{-1}, even though its sensitivity is not very high [33]. LIPSS generated on silicon substrates have been recently used as templates for gold deposition and SPR excitation, showing refractometric sensing capabilities with a FOM of 13.37 RIU^{-1} [34]. Therefore, our spectral sensitivity and FOM values (518 nm/RIU and 32 RIU^{-1}, respectively) are similar to those obtained using fabrication techniques that, in most cases, may require more complex fabrication steps and more expensive manufacturing tools than ours.

4. Conclusions

The use of femtosecond laser nanostructuring to generate LIPSS is a well-known and robust technology. A single laser processing generates a template for the deposition of conformal metallic layers. This capability has allowed the use of LIPSS to excite surface plasmon resonances. These resonances are commonly used in plasmonic devices for refractometric sensing. Then, by merging both well-established concepts – thin film coating of LIPSS plus plasmonic refractometry –, we have demonstrated a device that shows good refractometric performance in aqueous media, produced with a technology having a lower cost than other high-resolution nanofabrication tools. Even more, the actual profile of LIPSS depends on the fabrication parameters (number of pulses, energy delivered by each pulse, polarization state of the ablation beam, etc.) and the substrate characteristics. This flexibility makes possible the customization of LIPSS to increase the device sensitivity for specific ranges in index of refraction, wavelength, angle of incidence, or other environmental constrains.

In this work, we fabricate a sensing device based on split-LIPSS on stainless steel and coated with Au, and demonstrate its application in the refractometry of aqueous media. The profile takes the form of a hybrid structure between LIPSS and split-LIPSS, where the ripples of the profile shows a central dip. Our fabrication set-up produces LIPSS with high regularity over a large area and in a single laser pass. This has been possible by focusing the beam utilizing a cylindrical lens. A second fabrication step, consisting on Au sputtering and conformal deposition, enhances the response of SPR of the device. The whole manufacturing strategy constitutes a comparatively cheaper process with ample potential miniaturization capabilities. The design has been modeled using a computational electromagnetism package that reproduces the experimental results. Beyond the validation of the current data, this simulation makes possible to find profile parameters that could enhance the performance of similar devices and adapt the LIPSS morphology to other specific circumstances in refractometric sensing. Both the experimental and computational results are checked against a classical model of surface plasmon resonances coupled with a continuous spectral background. Fano-like line-shapes are successfully fitted to the spectral characteristics of the resonances, and determine the values of sensitivity and figure of merit. These two refractometric parameters are widely considered as describing the quality of the device and the sensing technology. As a result of this approach, our fabricated device shows a spectral sensitivity value of 518 nm/RIU and FOM of 32 RIU^{-1}. These values are very competitive when compared to similar devices fabricated with low-cost, and high-speed fabrication tools.

Declaration of competing interest

The authors declare that they have no known competing financial interests or personal relationships that could have appeared to influence the work reported in this paper.

Data availability

Data will be made available on request.

Acknowledgments

This work has been partially supported by Ministerio de Economía y Competitividad (Spain) and the European funds for regional development (EU): Retos Colaboración 2019, Teluro-AEI project, RTC2019-007113-3, and by project Nanorooms PID2019-105918GB-I00.

References

[1] A.K. Sharma, R. Jha, B.D. Gupta, Fiber-optic sensors based on surface plasmon resonance: A comprehensive review, IEEE Sens. J. 7 (8) (2007) 1118–1129, http://dx.doi.org/10.1109/JSEN.2007.897946.

[2] H. Esmaeilzadeh, E. Arzi, F. Légaré, M. Rivard, A. Hassani, A super continuum characterized high-precision SPR fiber optic sensor for refractometry, Sensors Actuators A 229 (2015) 8–14, http://dx.doi.org/10.1016/j.sna.2015.03.021.

[3] V. Yesudasu, H.S. Pradhan, R.J. Pandya, Recent progress in surface plasmon resonance based sensors: A comprehensive review, Heliyon 7 (3) (2021) http://dx.doi.org/10.1016/j.heliyon.2021.e06321.

[4] Q. Wang, N.-N. Du, W.-M. Zhao, L. Wang, X.-W. Cong, A.-S. Zhu, F.-M. Qiu, K.-K. Zhang, Highly sensitive U-shaped optical fiber refractometer based on Bi2O2Se-assisted surface plasmon resonance, IEEE Trans. Instrum. Meas. 9456 (c) (2021) http://dx.doi.org/10.1109/TIM.2021.3129871.

[5] D. Sarid, W.A. Challener, Modern Introduction To Surface Plasmons: Theory, Mathematica Modeling, and Applications, Cambridge University Press, 2010, http://dx.doi.org/10.1017/CBO9781139194846.

[6] N. Díaz-Herrera, A. González-Cano, D. Viegas, J.L. Santos, M.-C. Navarrete, Refractive index sensing of aqueous media based on plasmonic resonance in tapered optical fibres operating in the 1.5 μm region, Sensors Actuators B 146 (1) (2010) 195–198, http://dx.doi.org/10.1016/j.snb.2010.02.036, URL https://www.sciencedirect.com/science/article/pii/S0925400510001401.

[7] A. González-Cano, M.-C. Navarrete, Ó. Esteban, N. Díaz-Herrera, Plasmonic sensors based on doubly-deposited tapered optical fibers, Sensors 14 (3) (2014) 4791–4805, http://dx.doi.org/10.3390/s140304791, URL https://www.mdpi.com/1424-8220/14/3/4791.

[8] S. Rossi, E. Gazzola, P. Capaldo, G. Borile, F. Romanato, Grating-coupled surface plasmon resonance (GC-SPR) optimization for phase-interrogation biosensing in a microfluidic chamber, Sensors (Switzerland) 18 (5) (2018) http://dx.doi.org/10.3390/s18051621.

[9] Y. Chai, F. Li, J. Wang, P. Karvinen, M. Kuittinen, G. Kang, Enhanced sensing performance from trapezoidal metallic gratings fabricated by laser interference lithography, Opt. Lett. 47 (4) (2022) 1009–1012, http://dx.doi.org/10.1364/OL.450151, URL http://opg.optica.org/ol/abstract.cfm?URI=ol-47-4-1009.

[10] S. Long, J. Cao, Y. Wang, S. Gao, N. Xu, J. Gao, W. Wan, Grating coupled SPR sensors using off the shelf compact discs and sensitivity dependence on grating period, Sensors Actuators Rep. 2 (1) (2020) 100016, http://dx.doi.org/10.1016/j.snr.2020.100016.

[11] J. Bonse, S. Hohm, S.V. Kirner, A. Rosenfeld, J. Kruger, Laser-induced periodic surface structures-a scientific evergreen, IEEE J. Sel. Top. Quantum Electron. 23 (3) (2017) 9000615, http://dx.doi.org/10.1109/JSTQE.2016.2614183.

[12] J. Bonse, S.V. Kirner, J. Krüger, Laser-induced periodic surface structures (LIPSS), in: Handbook of Laser Micro- and Nano-Engineering, Springer International Publishing, Cham, 2020, pp. 1–59, http://dx.doi.org/10.1007/978-3-319-69537-2_17-2.

[13] J. Bonse, J. Krüger, S. Höhm, A. Rosenfeld, Femtosecond laser-induced periodic surface structures, J. Laser Appl. 24 (4) (2012) 042006, http://dx.doi.org/10.2351/1.4712658, arXiv:https://doi.org/10.2351/1.4712658.

[14] C. Florian, E. Skoulas, D. Puerto, A. Mimidis, E. Stratakis, J. Solis, J. Siegel, Controlling the wettability of steel surfaces processed with femtosecond laser pulses, ACS Appl. Mater. Interfaces 10 (42) (2018) 36564–36571, http://dx.doi.org/10.1021/acsami.8b13908, arXiv:https://doi.org/10.1021/acsami.8b13908.

[15] F. Fraggelakis, G. Giannuzzi, C. Gaudiuso, I. Manek-Hönninger, G. Mincuzzi, A. Ancona, R. Kling, Double- and multi-femtosecond pulses produced by birefringent crystals for the generation of 2D laser-induced structures on a stainless steel surface, Materials 12 (8) (2019) http://dx.doi.org/10.3390/ma12081257, URL https://www.mdpi.com/1996-1944/12/8/1257.

[16] J. Bonse, S. Gräf, Maxwell meets marangoni—A review of theories on laser-induced periodic surface structures, Laser Photonics Rev. 14 (2020) 2000215, http://dx.doi.org/10.1002/lpor.202000215.

[17] E. Stratakis, J. Bonse, J. Heitz, J. Siegel, G. Tsibidis, E. Skoulas, A. Papadopoulos, A. Mimidis, A.-C. Joel, P. Comanns, J. Krüger, C. Florian, Y. Fuentes-Edfuf, J. Solis, W. Baumgartner, Laser engineering of biomimetic surfaces, Mater. Sci. Eng. R 141 (2020) 100562, http://dx.doi.org/10.1016/j.mser.2020.100562, URL https://www.sciencedirect.com/science/article/pii/S0927796X20300206.

[18] A. San-Blas, M. Martinez-Calderon, E. Granados, M. Gómez-Aranzadi, A. Rodríguez, S.M. Olaizola, LIPSS manufacturing with regularity control through laser wavefront curvature, Surfaces Interfaces 25 (2021) http://dx.doi.org/10.1016/j.surfin.2021.101205.

[19] I. Gnilitskyi, T.J. Derrien, Y. Levy, N.M. Bulgakova, T. Mocek, L. Orazi, High-speed manufacturing of highly regular femtosecond laser-induced periodic surface structures: Physical origin of regularity, Sci. Rep. 7 (2017) 8485, http://dx.doi.org/10.1038/s41598-017-08788-z.

[20] L. Touahir, J. Niedziółł ka Jönsson, E. Galopin, R. Boukherroub, A.C. Gouget-Laemmel, I. Solomon, M. Petukhov, J.-N. Chazalviel, F. Ozanam, S. Szunerits, Surface plasmon resonance on gold and silver films coated with thin layers of amorphous silicon-carbon alloys, Langmuir 26 (8) (2010) 6058–6065, http://dx.doi.org/10.1021/la903896m.

[21] Y. Gutiérrez, A.S. Brown, F. Moreno, M. Losurdo, Plasmonics beyond noble metals: Exploiting phase and compositional changes for manipulating plasmonic performance, J. Appl. Phys. 128 (8) (2020).

[22] S. Hou, Y. Huo, P. Xiong, Y. Zhang, S. Zhang, T. Jia, Z. Sun, J. Qiu, Z. Xu, Formation of long- and short-periodic nanoripples on stainless steel irradiated by femtosecond laser pulses, J. Phys. D: Appl. Phys. 44 (50) (2011) http://dx.doi.org/10.1088/0022-3727/44/50/505401.

[23] M.H. Elshorbagy, L.M. Sánchez-Brea, J. Buencuerpo, J. del Hoyo, Á. Soria-García, V. Pastor-Villarrrubia, A. San-Blas, A. Rodríguez, S.M. Olaizola, J. Alda, Polarization conversion using customized subwavelength laser-induced periodic surface structures on stainless steel, Photonics Res. 10 (9) (2022) 2024–2031, http://dx.doi.org/10.1364/PRJ.454451.

[24] M.H. Elshorbagy, A. Cuadrado, G. González, F.J. González, J. Alda, Performance improvement of refractometric sensors through hybrid Plasmonic–Fano resonances, J. Lightwave Technol. 37 (13) (2019) 2905–2913, URL http://opg.optica.org/jlt/abstract.cfm?URI=jlt-37-13-2905.

[25] K.M. Mayer, J.H. Hafner, Localized surface plasmon resonance sensors, Chem. Rev. 111 (6) (2011) 3828–3857, http://dx.doi.org/10.1021/cr100313v, arXiv:https://doi.org/10.1021/cr100313v, PMID: 21648956.

[26] Q.-Q. Meng, X. Zhao, C.-Y. Lin, S.-J. Chen, Y.-C. Ding, Z.-Y. Chen, Figure of merit enhancement of a surface plasmon resonance sensor using a low-refractive-index porous silica film, Sensors 17 (8) (2017) http://dx.doi.org/10.3390/s17081846, URL https://www.mdpi.com/1424-8220/17/8/1846.

[27] D.R. Lide (Ed.), CRC Handbook of Chemistry and Physics, CRC Press, 2005, http://dx.doi.org/10.1021/ja906434c.

[28] S. Mamykin, I. Gnilitskyi, M. Dusheyko, T. DeVol, V. Bliznyuk, Femtosecond laser nano-structuring for surface plasmon resonance-based detection of uranium, Appl. Surf. Sci. 576 (2022) 151831, http://dx.doi.org/10.1016/j.apsusc.2021.151831, URL https://www.sciencedirect.com/science/article/pii/S0169433221028749.

[29] W. Su, Y. Luo, Y. Ding, J. Wu, Low-cost surface plasmon resonance refractive index sensor based on the metal grating in DVD-ROM disc, Sensors Actuators A 330 (2021) 112858, http://dx.doi.org/10.1016/j.sna.2021.112858, URL https://www.sciencedirect.com/science/article/pii/S0924424721003216.

[30] S. Long, E. Wang, M. Wu, H. Zhu, N. Xu, Y. Wang, J. Cao, Sensing absorptive fluids with backside illuminated grating coupled SPR sensor fabricated by nanoimprint technology, Sensors Actuators A 337 (2022) 113416, http://dx.doi.org/10.1016/j.sna.2022.113416, URL https://www.sciencedirect.com/science/article/pii/S0924424722000541.

[31] F.H. Saboor, S. Hadian-Ghazvini, H. Heidarzadeh, Design and performance simulation of a highly sensitive nano-biosensor based on a realistic array of plasmonic synthesized nanostructures, Photon. Nanostruct.: Fundam. Appl. 49 (2022) 100991, http://dx.doi.org/10.1016/j.photonics.2022.100991, URL https://www.sciencedirect.com/science/article/pii/S1569441022000013.

[32] A.K. Ghosh, S. Sarkar, L.J. Nebel, O. Aftenieva, V. Gupta, O. Sander, A. Das, J. Joseph, S. Wießner, T.A.F. König, A. Fery, Exploring plasmonic resonances toward "large-scale" flexible optical sensors with deformation stability, Adv. Funct. Mater. 31 (30) (2021) 2101959, http://dx.doi.org/10.1002/adfm.202101959, arXiv:https://onlinelibrary.wiley.com/doi/pdf/10.1002/adfm.202101959, URL https://onlinelibrary.wiley.com/doi/abs/10.1002/adfm.202101959.

[33] Y. Shen, K. He, Q. Zou, S. Xing, J. Huang, M. Zheng, X. She, C. Jin, Ultrasmooth gold nanogroove arrays: Ultranarrow plasmon resonators with linewidth down to 2 nm and their applications in refractive index sensing, Adv. Funct. Mater. 32 (10) (2022) 2108741, http://dx.doi.org/10.1002/adfm.202108741, arXiv:https://onlinelibrary.wiley.com/doi/pdf/10.1002/adfm.202108741, URL https://onlinelibrary.wiley.com/doi/abs/10.1002/adfm.202108741.

[34] M. Wu, N. Xu, E. Wang, S. Geng, H. Zhu, C. Liu, J. Cao, anogratings Fabricated by Wet Etching Assisted Femtosecond Laser Modification of Silicon for Surface Plasmon Resonance Sensing, Tech. rep., SSRN, 2022, http://dx.doi.org/10.2139/ssrn.4130111, URL https://ssrn.com/abstract=4130111.